

PARALLELIZATION OF A FINITE ELEMENT SOLVER FOR CHEMO-MECHANICAL COUPLED ANODE AND CATHODE PARTICLES IN LITHIUM-ION BATTERIES

RAPHAEL SCHOOF¹, GIUSEPPE F. CASTELLI² AND
WILLY DÖRFLER¹

¹ Institute of Applied and Numerical Mathematics (IANM)
Karlsruhe Institute for Technology (KIT)
76131 Karlsruhe, Germany

² Institute of Thermal Process Engineering (TVT)
Karlsruhe Institute for Technology (KIT)
76131 Karlsruhe, Germany

corresponding author e-mail: raphael.schoof@kit.edu

Key words: Lithium-Ion Battery, Adaptive Finite Element Method, Continuum Modeling, Parallelization, Numerical Simulation

Abstract. Two chemo-mechanical coupled models for electrode particles of lithium-ion batteries are compared. On the one hand a Cahn–Hilliard-type phase-field approach models lithium intercalation, phase separation and large deformations in phase transforming cathode materials like lithium iron phosphate. On the other hand a chemo-mechanical particle model for lithium intercalation and large deformations for an anode material such as silicon is studied. The comparison of two different ways to define the deformation gradient for the large deformation approach and the two different material properties lead to differences in the resulting quantities and equations for the coupling of the chemo-mechanical model. The usage of an adaptive solution algorithm as well as the parallelization of the finite element solver via the message passing interface concept results in a more reasonable computation time to perform two-dimensional simulations. Both materials are numerically investigated and the results are compared from a physical point of view. When fast charging a battery, higher stress values are reached, which can cause a shorter cycle life. A strong scalability analysis shows good performance for the assembling, however a saturation occurs in the performance of the solver used.

1 INTRODUCTION

Due to a higher energy density and the longevity of lithium-ion batteries, they have become the standard for mobile applications [22]. To meet the challenges of climate change they are also crucial in overcoming the difficulties in the mobility transition to sustainable transport. However, the stress development, which can deteriorate the battery active material resulting in faster aging and shorter battery lifetime [24, 25, 26], is an important aspect to investigate during battery operation. This is also one crucial issue for fast charging batteries, e.g., for electric

vehicles [22]. Silicon (Si) as anode material has the advantage of an even further increase of the energy density, but this results at the cost of an increase in volume up to 300% [25, 26]. Other materials like graphite or lithium iron phosphate Li_xFePO_4 (LFP) feature a volume expansion during intercalation of lithium up to 10% and 7%, respectively [17, 26]. Due to the large swelling, in particular for silicon, the large deformation approach is a reasonable choice to model chemo-mechanical intercalation effects during battery operation. Interested readers are referred to [26] and the references therein for a detailed overview of electro-chemo-mechanical modeling of lithium-ion batteries.

There are various possibilities to handle the order of the decomposition of the deformation gradient due to chemical effects, elasticity or even further plasticity, compare [1, 10, 12, 15] and the references therein. In [9, 11], the deformation gradient \mathbf{F} is decomposed into $\mathbf{F}_{\text{el}}\mathbf{F}_{\text{ch}}$. Another possibility is given by the composition in the reverse order $\mathbf{F} = \mathbf{F}_{\text{ch}}\mathbf{F}_{\text{el}}$, as illustrated in Figure 1 in [23]. Both variants are thermodynamically consistent [9, 23]. The latter one has the advantage that it is easier to include a further plastic deformation before the elastic part such as $\mathbf{F}_{\text{el}}\mathbf{F}_{\text{pl}}$ and to hold the reversible part $\mathbf{F}_{\text{rev}} = \mathbf{F}_{\text{ch}}\mathbf{F}_{\text{el}}$ together.

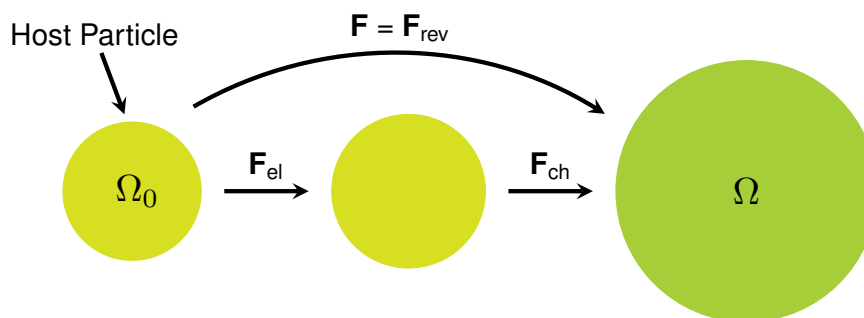


Figure 1: Sketch of the used decomposition of the deformation gradient based on Figure 1 in [23] and Figure 1 in [9].

Especially for materials with phase separation, numerical simulations are cost-intensive in terms of computational resources, because a small mesh size and a small time step size are required to adequately capture all physical effects. With the space and time adaptive solution algorithm developed in [6], this disadvantage is circumvented. Furthermore, a parallelization of the numerical algorithm for up-to-date high performance computers (HPCs) should lead to additional resource savings. In this work, the parallelization of the numerical solution algorithm is considered for anode materials like silicon without a phase separation after the first cycles [26] as well as for cathode materials with a phase separation such as LFP [20]. The effects of fast charging batteries on the stresses inside a particle are studied and compared with the stresses that occur during phase separation of LFP. All numerical experiments are performed for two-dimensional computational domains. Further, a strong scalability analysis study is executed to evaluate the efficiency of the parallelization.

This work is structured as follows: in Section 2, the theory used for the modeling approach is introduced. Then the general aspects of the numerical implementation are declared in Section 3. The specification for the numerical experiments as well as the simulation results are presented and discussed in Section 4. Finally, this work is summarized in Section 5.

2 THEORY

This section gives a short overview on the two different approaches for the deformation gradient and their consequences for the whole system. In addition, the differences for materials with phase separation, following Section 2 in [9], and for materials without phase separation, following Section 2.1 in [23], are shown. For more information see also the supporting information of [23].

Large deformation approach. Following Figure 1, there is a reference Lagrangian domain Ω_0 and the Eulerian domain Ω which are related by the mapping $\mathbf{x} : \Omega_0 \rightarrow \Omega$. This defines the total deformation gradient $\mathbf{F} = \partial \mathbf{x} / \partial \mathbf{X}_0$, which can also be written such as $\mathbf{F} = \mathbf{Id} + \nabla \mathbf{u}$ with the deformation \mathbf{u} and the identity matrix \mathbf{Id} [4, 13]. As discussed in the introduction, the reversible total particle deformation can be multiplicatively decomposed into an elastic part \mathbf{F}_{el} representing mechanical stresses and a chemical part \mathbf{F}_{ch} resulting from changes in lithium concentration:

$$\mathbf{F} = \mathbf{F}_{\text{rev}} = \mathbf{F}_{\text{ch}} \mathbf{F}_{\text{el}}. \quad (1)$$

Free energy density. With a thermodynamically consistent model based on a free energy density ψ , a strictly positive entropy production is guaranteed [18]. We use the free energy density ψ defined by two parts: a chemical part ψ_{ch} and an elastic part ψ_{el} . For modeling materials with phase separation as in [9], the energy density has to be extended by an interfacial part ψ_{int} . If no phase separation occurs, the chemical part ψ_{ch} has to be adapted since the double-well function, used for materials with phase separation, has to be replaced. Instead, the open circuit voltage (OCV) curve U_0 of the specific material is used:

$$\psi_{\text{ch}}(c) = - \int_0^c F U_0(z) dz \quad (2)$$

with the normalized concentration c (normalized with c_{max}) and the Faraday constant F . The elastic part ψ_{el} follows the same linear elastic approach as in [4, 9, 13, 23]. The elastic strain tensor \mathbf{E}_{el} for our model is defined by

$$\mathbf{E}_{\text{el}} = \frac{1}{2} \left(\mathbf{F}_{\text{el}}^T \mathbf{F}_{\text{el}} - \mathbf{Id} \right) = \frac{1}{2} \left(\lambda_{\text{ch}}^{-2} \mathbf{F}^T \mathbf{F} - \mathbf{Id} \right), \quad (3)$$

which differs from the approach where the two deformation gradients are defined in the reverse order. In that case, the elastic strain tensor \mathbf{E}_{el} is given by $\mathbf{E}_{\text{el}} = \frac{1}{2} \left(\mathbf{F}^T \mathbf{F} - \mathbf{F}_{\text{ch}}^T \mathbf{F}_{\text{ch}} \right) = \frac{1}{2} \left(\mathbf{F}^T \mathbf{F} - \lambda_{\text{ch}}^2 \mathbf{Id} \right)$.

Chemistry. The change of the lithium concentration inside the host material can be defined with the continuity equation

$$\partial_t c = -\nabla \cdot \mathbf{N}, \quad (4)$$

where $\mu = \partial_c \psi$ is the chemical potential, $\mathbf{N} = -D (\partial_c \mu)^{-1} \nabla \mu$ the lithium flux and D the diffusion coefficient. The lithium flux \mathbf{N} is chosen to guarantee positive entropy production [23]. The simulation time t and the state of charge (SOC) can be related by

$$\text{SOC} = \frac{1}{V} \int_{\Omega_0} c d\mathbf{X}_0 = c_0 + N_{\text{ext}} \cdot t \quad (5)$$

with a constant normalized initial condition c_0 .

Elastic deformation. The momentum balance in the Lagrangian frame

$$\mathbf{0} = -\nabla \cdot \mathbf{P} \quad (6)$$

models the mechanical deformation, where $\mathbf{P} = \det(\mathbf{F}) \sigma \mathbf{F}^{-\top}$ is the first Piola–Kirchhoff stress tensor and σ the Cauchy stress in the Eulerian frame. Further, \mathbf{P} can be described by

$$\mathbf{P} = \partial_{\mathbf{F}} \psi = \lambda_{\text{ch}}^{-2} \mathbf{F} \mathbf{C} \mathbf{E}_{\text{el}}. \quad (7)$$

Equation (7) differs by the factor λ_{ch}^{-2} from the approach with the reverse order of the deformation gradient parts.

3 NUMERICAL PROCEDURE

In this section, we briefly discuss all important aspects regarding the numerical treatment, e.g., the normalization of the model parameters, the problem formulation as well as the space and time discretization of the used adaptive numerical solution algorithm. Overall, the space and time adaptive solution algorithm of [9] is applied. For further details on the numerical method refer to [6].

Normalization. For the normalization of the basic model parameters, refer to Section 3.1.1 in [9] and, in addition, use F/RT as normalization for the OCV function U_0 with the gas constant R and the reference operation temperature T .

Problem statement. The resulting dimensionless initial boundary value problem for the discussed model from Section 2 is given as: Let $t_{\text{end}} > 0$ the final simulation time and $\Omega_0 \subset \mathbb{R}^d$ a bounded electrode particle as reference configuration with dimension $d \in \{1, 2, 3\}$. Find the concentration $c: [0, t_{\text{end}}] \times \bar{\Omega}_0 \rightarrow [0, 1]$, the chemical potential $\mu: [0, t_{\text{end}}] \times \bar{\Omega}_0 \rightarrow \mathbb{R}$ and the displacement $\mathbf{u}: [0, t_{\text{end}}] \times \bar{\Omega}_0 \rightarrow \mathbb{R}^d$ satisfying

$$\left\{ \begin{array}{ll} \partial_t c = -\nabla \cdot \mathbf{N} & \text{in } (0, t_{\text{end}}) \times \Omega_0, \\ \mu = \partial_c \psi & \text{in } (0, t_{\text{end}}) \times \Omega_0, \\ 0 = -\nabla \cdot \mathbf{P} & \text{in } (0, t_{\text{end}}) \times \Omega_0, \\ \nabla c \cdot \mathbf{n} = 0 & \text{on } (0, t_{\text{end}}) \times \partial\Omega_0, \\ \mathbf{N} \cdot \mathbf{n} = N_{\text{ext}} & \text{on } (0, t_{\text{end}}) \times \partial\Omega_0, \\ \mathbf{P} \cdot \mathbf{n} = \mathbf{0} & \text{on } (0, t_{\text{end}}) \times \partial\Omega_0, \\ c(0, \cdot) = c_0 & \text{in } \Omega_0 \end{array} \right.$$

with the outer unit normal vector \mathbf{n} of the reference configuration, a constant external lithium flux N_{ext} and an initial condition c_0 , which is consistent with the boundary conditions. Rigid body motions are excluded by using appropriate boundary conditions for the deformation.

Numerical solution algorithm. The finite element method is used for the spatial discretization of the above stated model equations, which are solved with the developed adaptive solution algorithm from [9]. However, note the following changes: the omitted interfacial energy ψ_{int} , the change in the chemical energy ψ_{ch} and the lithium flux \mathbf{N} . The resulting nonlinear differential algebraic equation (DAE) is linearized with a Newton–Raphson method and is solved

in time by using a variable-step, variable-order algorithm [19]. The Newton updates are computed with a direct LU-decomposition. A gradient recovery estimator serves as a local criterion for the adaptive mesh refinement and coarsening. For further details refer to [6, 7, 8, 9], especially the solver validation in Section 4.3.1 and adaptivity results in Section 4.3.2, both in [9].

4 NUMERICAL INVESTIGATIONS

In the following section we describe the simulation setup and discuss our numerical results.

4.1 Simulation setup

In this subsection we first specify the particle geometries and the model parameters. Then implementation details are given.

Model parameters. For all simulations, the model parameters can be found in Table 1 if not otherwise specified. The open circuit voltage (OCV) function U_0 for silicon is given by

$$U_0(z) := \frac{-0.2453z^3 - 0.00527z^2 + 0.2477z + 0.006457}{z + 0.002493} \quad (8)$$

displayed in Figure 2 [23].

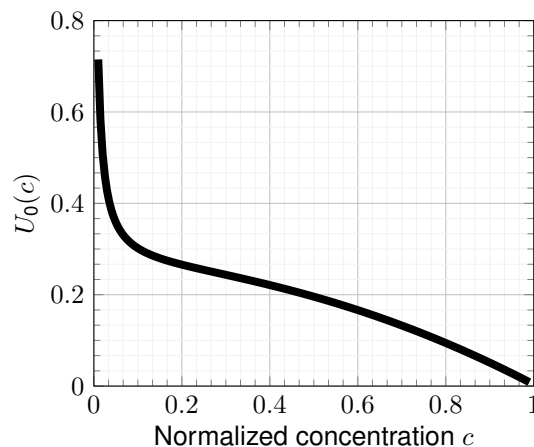


Figure 2: OCV curve U_0 for silicon over the normalized concentration $c \in [0.01, 0.99]$ [23].

Particle geometries. Two particle geometries are investigated: a two-dimensional quarter domain of a cross-section of a spheroidal particle and a two-dimensional quarter domain of a cross-section of a spherical particle. For the first case, refer to Figure 3 in [9]. The second case is similar to the first one but has equal axes ratio. This configuration follows the shape of silicon nano pillars [26].

Implementation. The implementation of the numerical methods are based on the functionalities of the finite element library *deal.II* [2] written in C++. Furthermore, fourth-order isoparametric Lagrangian finite elements are used for all numerical simulations. The simulations are solved with *SuperLU-DIST* [16]. Finally, the adaptive solution algorithm is parallelized using Message Passing Interface (MPI) for parallel computing architectures. We use the parallel

Table 1: Model parameters for numerical experiments [9, 23].

Description	Symbol	Value	Unit	Dimensionless
Universal gas constant	R	8.314	$\text{J mol}^{-1} \text{K}^{-1}$	1
Faraday constant	F	96 485	$\text{J V}^{-1} \text{mol}^{-1}$	1
Operation temperature	T	298.15	K	1
LFP				
Particle length scale	L_0	150×10^{-9}	m	1
Diffusion coefficient	D	1×10^{-14}	$\text{m}^2 \text{s}^{-1}$	1.6×10^3
Coefficient for ψ_{ch}	α_1	4.5	-	4.5
Coefficient for ψ_{ch}	α_2	-9	-	-9
Coefficient for ψ_{int}	κ	8.8×10^{-18}	m^2	3.91×10^{-4}
Young's modulus	E_{H}	124.5×10^9	Pa	2.23×10^3
Poisson ratio	ν	0.25	-	0.25
Partial molar volume	v	2.9×10^{-6}	$\text{m}^3 \text{mol}^{-1}$	3.41
Maximal concentration	c_{max}	2.29×10^4	mol m^{-3}	1
Initial concentration	c_0	2.29×10^2	mol m^{-3}	1×10^{-2}
Silicon				
Particle length scale	L_0	50×10^{-9}	m	1
Diffusion coefficient	D	1×10^{-17}	$\text{m}^2 \text{s}^{-1}$	14.4
Open circuit voltage (OCV)	U_0	Equation (8)	V	$F/RT \cdot (8)$
Young's modulus	E_{H}	90.13×10^9	Pa	116.74
Poisson ratio	ν	0.22	-	0.22
Partial molar volume	v	10.96×10^{-6}	$\text{m}^3 \text{mol}^{-1}$	3.41
Maximal concentration	c_{max}	311.47×10^3	mol m^{-3}	1
Initial concentration	c_0	3.11×10^3	mol m^{-3}	1×10^{-2}

capabilities of deal.II implemented through the interface to p4est [3] to distribute the mesh on distributed memory and the Trilinos wrapper package for parallel solvers to solve the linear system [21]. The simulations were performed on a single compute node of the BwUniCluster 2.0 with 40 Intel Xeon Gold 6230 with 2.1 GHz and 96 GB RAM [5].

4.2 Numerical results

This subsection deals with the discussion of performed numerical simulations, in particular with the parallelization of the finite element solver and the comparison of two-dimensional anode and cathode particles. For the cathode particles, LFP is used as simulated material and the theory of [9] is applied.

Parallelization. With the parallelization of the finite element solver for HPCs using MPI, the computational domain is distributed over the number of available CPUs. For the start of the numerical simulation, the decomposition of the computational domain is displayed in Figure 3a. The domain is uniformly refined and each CPU is connected to a spatially similar area to handle approximately the same workload. During the simulation of LFP, lithium is intercalated into the particle and the domain is adaptively refined within the areas of high gradients, i.e. within the areas of the phase front. This results in a redistribution of the area one CPU is connected to, because each CPUs has to deal with the similar number of degrees of freedom (DOFs). This redistribution also continues in the further development of the simulation, compare Figure 3b-d. For a concentration development see Figure 10 in [9].

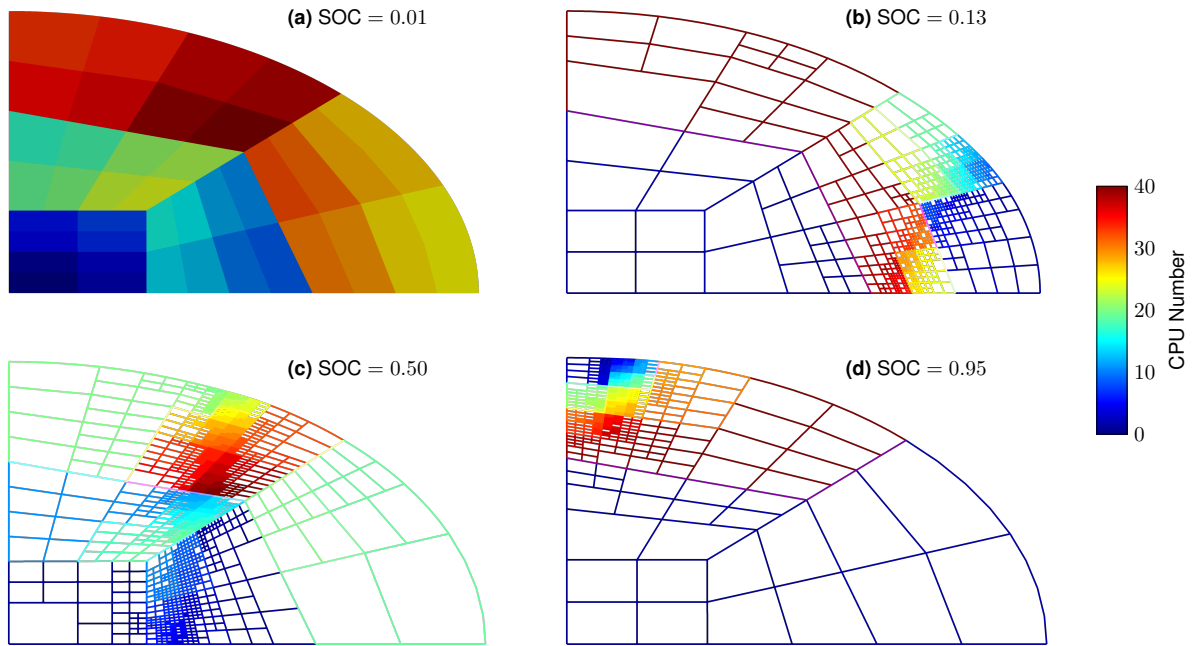


Figure 3: Decomposition of the computational domain for each CPU using a parallelization of the finite element solver for different SOC levels with an adaptively refined mesh for a full lithiation of a particle.

Large deformation. As mentioned in the introduction, the anode material silicon has a larger volume expansion compared to the cathode material LFP. This difference can also be detected in Figure 4 in comparison to Figure 3. In both figures the computational domain is warped by the displacement field \mathbf{u} . This leads to a larger growth in the silicon domain compared to LFP. In particular, note the large growth of the particle size during the intercalation of lithium into the particle, displayed Figure 4a-d. Therefore, the large deformation approach, used in the theory Section 2, is justified and a small deformation theory like in [14] would not be an appropriate choice in this case. Due to the spatial adaptivity, the number of cells can be reduced, so if the problem size is too small to be distributed over all available CPUs, some CPUs will not be used.

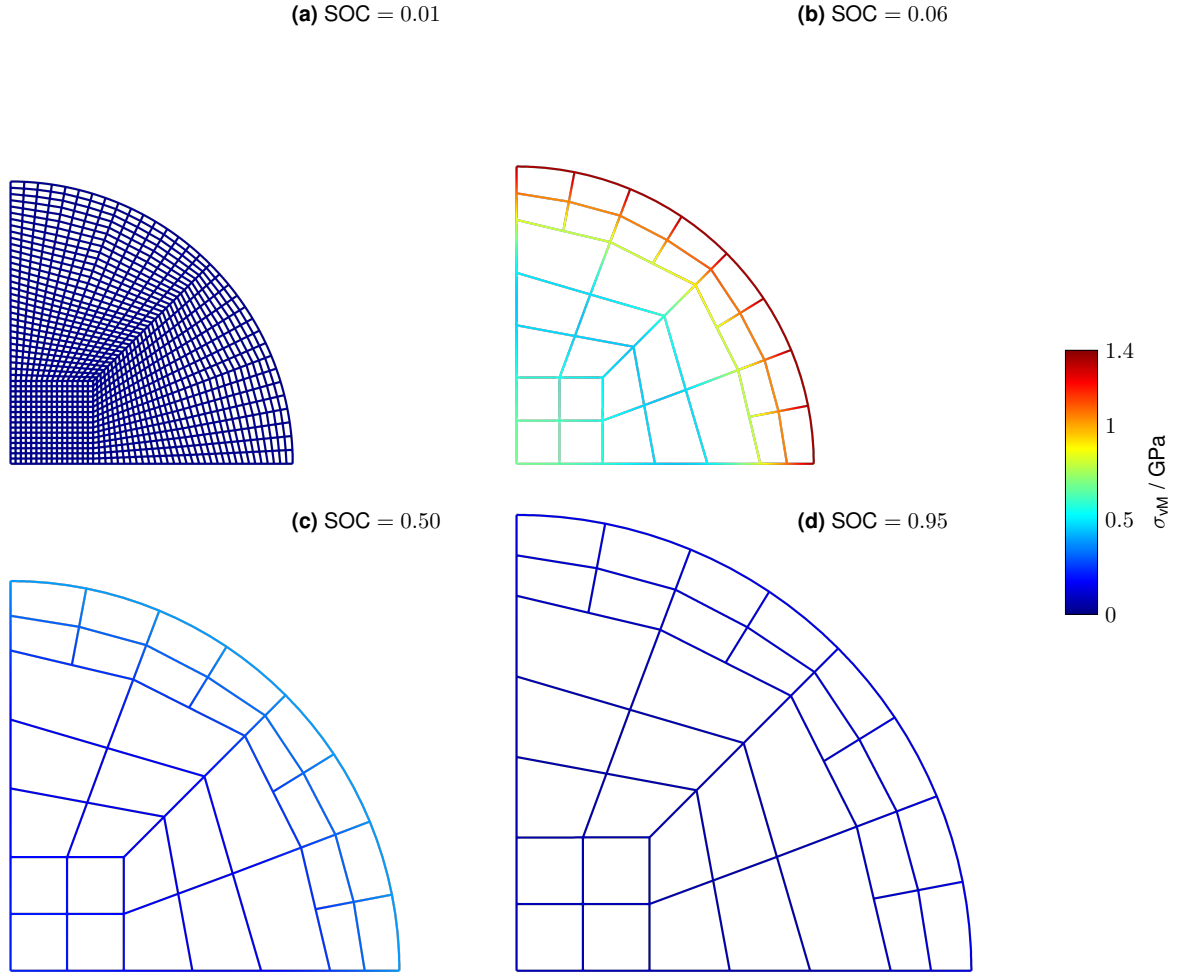


Figure 4: Full lithiation of a particle resulting in large deformations for silicon as anode material and development of von Mises stresses σ_{vM} in GPa for different SOC.

Stress development. Indicated by the colorbar, Figure 4 shows the development of the *von Mises stress* σ_{vM} in the general plane state defined by

$$\sigma_{vM} = \sqrt{\sigma_{11}^2 + \sigma_{22}^2 - \sigma_{11}\sigma_{22} + 3\sigma_{12}^2}. \quad (9)$$

In the beginning of the intercalation of lithium into the host material, the von Mises stress increases to its maximum around 1.4 GPa in Figure 4b and then decreases again. The maximum of the von Mises stress over the total simulation is displayed in Figure 5 in blue. The reason for the peak value at this early stage is the strong gradient in the OCV for silicon (Equation (8), Figure 2). The change from larger gradient values of the OCV function U_0 to smaller ones leads to a larger lithium flux and a higher concentration gradient resulting in larger stresses.

Totally different is the profile of the von Mises stresses for LFP, where three things are eye catching: Firstly, two peaks (one at the beginning and one at the end), secondly (apart from

that two peaks) a plateau in middle area of the simulation and thirdly nearly no stress at the start and at the very end of the simulation. The last point can be explained by the fact that in these cases the concentration is nearly constant and has approximately a zero gradient, resulting in an almost not visible stress. The higher stress values during the plateau area are related to the migration of the phase separation that moves from the area of highest curvature on the right corner to the top left corner of the computational domain. The first stress peak can be explained by the fact that for a short moment two further phase fronts emerge in the area of the top left corner. Due to the displacement constraints on the short half axis of the computational domain, one of two emerging phase fronts near to the short half axis causes the high stress. The displacement constraints are also the reason for the second peak just before SOC = 0.8, where the remaining phase front passes through the lower left corner, the center of the spheroidal particle under consideration.

The green graph in Figure 5 is simulated with the silicon parameters of Table 1 and the Fourier number $Fo = 2.88$. The Fourier number describes the ratio of the diffusive transport rate to the storage rate. A smaller Fourier number can therefore be interpreted as a use case for fast charging. This results in a stretched curve of the stress values in comparison to the usual application being even higher than the stress values for phase separation case. Fast charging therefore implies large stresses inside a particle, which can cause particle fracture and have a negative effect on the aging of lithium-ion batteries.

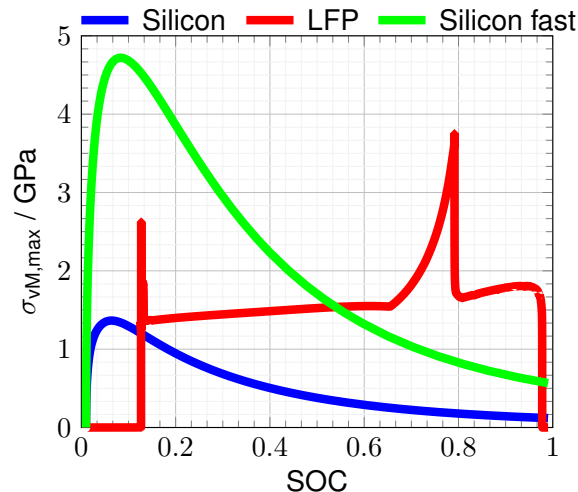


Figure 5: Maximal von Mises stresses in GPa of the total domain over the SOC for silicon, LFP and silicon with a smaller Fourier number, representing fast charging.

Solver scalability analysis. The parallelization of the finite element solver should lead to a corresponding time saving for the total simulation time. To investigate the strong parallel scalability behavior, the mesh is uniformly refined to consider a sufficient large problem size with approximately 1.4 million DOFs for the LFP simulation setup with a full ellipse and $t_{\text{end}} = 0.17$. The results of the time measurements are shown in Figure 6. The assembling of the linearized systems in each Newton step including the Jacobian and the residual shows nearly optimal linear scaling with increase of the CPU number. However, the time for solving the linear system

saturates and clearly shows a bottleneck in the performance. This has an impact on the total simulation time, which also runs into saturation. This means that the overall parallel scaling is dominated by the saturation due to the direct LU decomposition through superLU_Dist. A more scalable parallel solver can circumvent this issue.

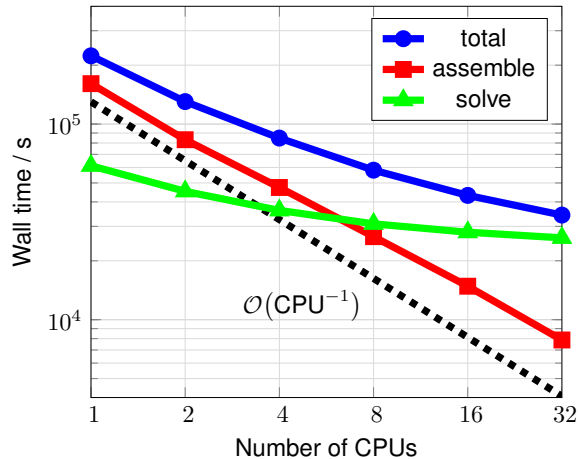


Figure 6: Computational wall clock time in seconds for the total simulation, the assembly and the solution of the linear system for different numbers of CPUs. The dashed black line indicates optimal scaling.

5 CONCLUSIONS AND OUTLOOK

In summary, we have used two thermodynamically consistent chemo-mechanical models to analyze the intercalation of lithium in anode and cathode battery particles. For this the two modeling approaches of [9] and [23] were compared and the differences for materials with and without phase separation were marked out. Especially, the order of the multiplicative decomposition of the deformation gradient vector was discussed and both options were declared admissible, since both ways are thermodynamically consistent. Further numerical investigations on this comparison will be executed.

The adaptivity together with the MPI parallelization of the finite element solver allows to compute two-dimensional domains for silicon as anode material and LFP as cathode material within a shorter, more reasonable time. The alteration of the distribution of computational area to the respective CPU during the intercalation of lithium into the particle was pointed out. An anode material such as silicon shows a larger volume expansion than the cathode material LFP. This was confirmed by two-dimensional simulations for the respective material. Reducing the Fourier number illustrates a problem for the current issue of fast charging lithium-ion batteries, e.g., for mobility transition. Fast charging leads to larger stresses and can even result in particle fracture which has a decisive effect on the health and aging of the battery. Therefore, additional effects like plasticity and fracture should be added to the modeling approach. The strong scaling analysis revealed a saturation for solving the linear system with the direct LU decomposition through superLU_Dist. The development of a parallel scalable solver is part of the current research in our group. With an adapted solver, the faster computation of even three-dimensional, arbitrarily shaped geometries is a promising research topic.

Acknowledgments

R.S. and F.C. acknowledge financial support by the German Research Foundation (DFG) through the Research Training Group 2218 SiMET – Simulation of mechano-electro-thermal processes in lithium-ion batteries, project number 281041241.

This work was performed on the computational resource bwUniCluster funded by the Ministry of Science, Research and the Arts Baden-Württemberg and the Universities of the State of Baden-Württemberg, Germany, within the framework program bwHPC.

ORCID

Raphael Schoof <https://orcid.org/0000-0001-6848-3844>

Giuseppe F. Castelli <https://orcid.org/0000-0001-5484-6093>

Willy Dörfler <https://orcid.org/0000-0003-1558-9236>

REFERENCES

- [1] L. Anand. A Cahn–Hilliard-type theory for species diffusion coupled with large elastic–plastic deformations. *Journal of the Mechanics and Physics of Solids*, 60(12):1983–2002, 2012. doi:10.1016/j.jmps.2012.08.001.
- [2] D. Arndt, W. Bangerth, B. Blais, M. Fehling, R. Gassmöller, T. Heister, L. Heltai, U. Köcher, M. Kronbichler, M. Maier, P. Munch, J.-P. Pelteret, S. Proell, K. Simon, B. Turcksin, D. Wells, and J. Zhang. The deal.II library, Version 9.3. *Journal of Numerical Mathematics*, 29(3):171–186, 2021. doi:10.1515/jnma-2021-0081.
- [3] W. Bangerth, C. Burstedde, T. Heister, and M. Kronbichler. Algorithms and Data Structures for Massively Parallel Generic Adaptive Finite Element Codes. *ACM Transactions on Mathematical Software*, 38(2):14:1–14:28, 2011. doi:10.1145/2049673.2049678.
- [4] D. Braess. *Finite Elements*. Cambridge University Press, Cambridge, third edition, 2007.
- [5] WIKI bw HPC Team. *BwUniCluster 2.0 Hardware and Architecture*, 2022. URL https://wiki.bwhpc.de/e/BwUniCluster_2.0_Hardware_and_Architecture.
- [6] G. F. Castelli. *Numerical Investigation of Cahn–Hilliard-Type Phase-Field Models for Battery Active Particles*. PhD thesis, Karlsruhe Institute of Technology (KIT), 2021. doi:10.5445/IR/1000141249.
- [7] G. F. Castelli and W. Dörfler. A parallel matrix-free finite element solver for phase separation in electrode particles of lithium ion batteries. *Proceedings in Applied Mathematics & Mechanics 2021*, 21(1):e202100169, 2021. doi:10.1002/pamm.202100169.
- [8] G. F. Castelli and W. Dörfler. Study on an adaptive finite element solver for the Cahn–Hilliard equation. In F. J. Vermolen and C. Vuik, editors, *Numerical Mathematics and Advanced Applications ENUMATH 2019*, volume 139 of *Lecture Notes in Computational Science and Engineering*, pages 245–253. Springer, Cham, 2021. doi:10.1007/978-3-030-55874-1_23.
- [9] G. F. Castelli, L. von Kolzenberg, B. Horstmann, A. Latz, and W. Dörfler. Efficient Simulation of Chemical-Mechanical Coupling in Battery Active Particles. *Energy Technology*, 9(6):2000835, 2021. doi:10.1002/ente.202000835.
- [10] Z. Cui, F. Gao, and J. Qu. A finite deformation stress-dependent chemical potential and its applications to lithium ion batteries. *Journal of the Mechanics and Physics of Solids*, 60(7):1280–1295, 2012. doi:10.1016/j.jmps.2012.03.008.

- [11] Y. F. Gao and M. Zhou. Strong dependency of lithium diffusion on mechanical constraints in high-capacity li-ion battery electrodes. *Acta Mechanica Sinica*, 28(4):1068–1077, 2012. doi:10.1007/s10409-012-0141-4.
- [12] Y. F. Gao, M. Cho, and M. Zhou. Stress relaxation through interdiffusion in amorphous lithium alloy electrodes. *Journal of the Mechanics and Physics of Solids*, 61(2):579–596, 2013. doi:10.1016/j.jmps.2012.09.004.
- [13] G. A. Holzapfel. *Nonlinear Solid Mechanics*. John Wiley & Sons, Ltd., Chichester, 2000.
- [14] M. Huttin and M. Kamlah. Phase-field modeling of stress generation in electrode particles of lithium ion batteries. *Applied Physics Letters*, 101(13):133902–1–133902–4, 2012. doi:10.1063/1.4754705.
- [15] E. H. Lee. Some comments on elastic-plastic analysis. *International Journal of Solids and Structures*, 17(9):859–872, 1981. doi:10.1016/0020-7683(81)90101-3.
- [16] X. S. Li and J. W. Demmel. SuperLU_DIST: A Scalable Distributed-Memory Sparse Direct Solver for Unsymmetric Linear Systems. *ACM Transactions on Mathematical Software*, 29(2):110–140, June 2003. doi:10.1145/779359.779361.
- [17] T. V. S. L. Satyavani, A. Srinivas Kumar, and P. S. V. Subba Rao. Methods of synthesis and performance improvement of lithium iron phosphate for high rate Li-ion batteries: A review. *Engineering Science and Technology, an International Journal*, 19(1):178–188, 2016. doi:10.1016/j.jestch.2015.06.002.
- [18] M. Schammer, B. Horstmann, and A. Latz. Theory of Transport in Highly Concentrated Electrolytes. *Journal of The Electrochemical Society*, 168(2):026511, 2021. doi:10.1149/1945-7111/abddd.
- [19] L. F. Shampine and M. W. Reichelt. The MATLAB ODE Suite. *SIAM Journal on Scientific Computing*, 18(1):1–22, 1997. doi:10.1137/S1064827594276424.
- [20] V. Srinivasan and J. Newman. Discharge Model for the Lithium Iron-Phosphate Electrode. *Journal of The Electrochemical Society*, 151(10):A1517, 2004. doi:10.1149/1.1785012.
- [21] The Trilinos Project Team. *The Trilinos Project Website*, 2020 (accessed May 22, 2020). URL <https://trilinos.github.io>.
- [22] A. Tomaszewska, Z. Chu, X. Feng, S. O’Kane, X. Liu, J. Chen, C. Ji, E. Endler, R. Li, L. Liu, Y. Li, S. Zheng, S. Vetterlein, M. Gao, J. Du, M. Parkes, M. Ouyang, M. Marinescu, G. Offer, and B. Wu. Lithium-ion battery fast charging: A review. *eTransportation*, 1:100011, 2019. doi:10.1016/j.etrans.2019.100011.
- [23] L. von Kolzenberg, A. Latz, and B. Horstmann. Chemo-Mechanical Model of SEI Growth on Silicon Electrode Particles. *Battery & Supercaps*, 5(2):e202100216, 2022. doi:10.1002/batt.202100216.
- [24] R. Xu and K. Zhao. Electrochemomechanics of Electrodes in Li-Ion Batteries: A Review. *Journal of Electrochemical Energy Conversion and Storage*, 13(3):030803, 12 2016. doi:10.1115/1.4035310.
- [25] W.-J. Zhang. A review of the electrochemical performance of alloy anodes for lithium-ion batteries. *Journal of Power Sources*, 196(1):13–24, 2011. doi:10.1016/j.jpowsour.2010.07.020.
- [26] Y. Zhao, P. Stein, Y. Bai, M. Al-Siraj, Y. Yang, and B.-X. Xu. A review on modeling of electro-chemo-mechanics in lithium-ion batteries. *Journal of Power Sources*, 413:259–283, 2019. doi:10.1016/j.jpowsour.2018.12.011.